Emergent dynamic chirality in a thermally driven artificial spin ratchet

Sebastian Gliga[1,2,3,*], Gino Hrkac[4], Claire Donnelly[2,3], Jonathan Büchi[2], Armin Kleibert[3], Jizhai Cui[2,3], Alan Farhan[2,3,5], Eugenie Kirk[2,3], Rajesh V. Chopdekar[6], Yusuke Masaki[7], Nicholas S. Bingham[2,3,8], Andreas Scholl[5], Robert L. Stamps[1], Laura J. Heyderman[2,3]

1 SUPA, School of Physics and Astronomy, University of Glasgow, Glasgow, G12 8QQ, United Kingdom.

2 Laboratory for Mesoscopic Systems, Department of Materials, ETH Zurich, 8093 Zurich, Switzerland.

3 Paul Scherrer Institut, 5232 Villigen PSI, Switzerland.

4 College of Engineering, Mathematics and Physical Sciences, University of Exeter, Exeter, EX4 4QF, United Kingdom.

5 Advanced Light Source, Lawrence Berkeley National Laboratory (LBNL), 1 Cyclotron Road, Berkeley, California 94720, USA.

6 Department of Materials Science and Engineering, University of California, Davis, Davis, CA 95616, USA.

7 Department of Physics, The University of Tokyo, Tokyo, 113-0033, Japan.

8 National Research Council Research Associate at the U.S. Naval Research Laboratory 4555 Overlook Ave., SW Washington, DC 20375.

Modern nanofabrication techniques have opened the possibility to create novel functional materials, whose properties transcend that of their constituent elements. In particular, tuning the magnetostatic interactions in geometrically-frustrated arrangements of nanoelements called artificial spin ice[1,2] can lead to specific collective behaviour[3] including emergent magnetic monopoles[4,5], charge screening[6,7] and transport[8,9] as well as magnonic response[10-12]. Here, we demonstrate a spin-ice based active material in which energy is converted into unidirectional dynamics. Using x-ray photoemission electron microscopy we show that the collective rotation of the average magnetisation proceeds in a unique sense during thermal relaxation. Our simulations demonstrate that this emergent chiral behaviour is driven by the topology of the magnetostatic field

at the edges of the nanomagnet array, resulting in an asymmetric energy landscape. In addition, a bias field can be used to modify the sense of rotation of the average magnetisation. This opens the possibility of implementing a magnetic Brownian ratchet[13-14], which may find applications in novel nanoscale devices, such as magnetic nanomotors, actuators, sensors or memory cells.

Chirality is a ubiquitous phenomenon in nature present in a variety of systems, from elementary particles, through the charge-parity violation of the weak interaction, to biomolecules whose function is defined by their handedness. In artificial systems, such as optical metamaterials, structural chirality can be exploited to control light-matter interactions and produce circularly polarized light[15]. In ferromagnets and antiferromagnets, the Dzyaloshinskii-Moriya interaction can give rise to chiral spin textures[16] and lead to non-reciprocal dynamics[17]. While most studied phenomena rely on a static view of chirality – *Is a system superimposable to its mirror image?* – this definition can be extended to include electric and magnetic fields as well as dynamic properties[18]. In this context, *dynamic* chirality is a property of both chiral as well as achiral objects that display a preferred sense of rotation. In classical mechanics, an example is the rattleback: a spinning top that only rotates in one direction, while in chemistry, the interactions between an adsorbed molecule and a crystal surface can lead to the rotation of the molecule in a preferred direction[19].

Here we present an example of emergent dynamic chirality in an artificial spin ice system – a 'chiral ice'. Schematically represented in Fig. 1, the system consists of a two-dimensional arrangement of lithographically patterned single-domain nanomagnets in which the magnetisation points in one of two orientations along the magnet long axis due to shape anisotropy[1]. The choice of the array design is such that it is structurally chiral, *i.e.* it cannot be superimposed onto its mirror image, when considering the edges of the array. The two-dimensional character of the system is constrained by the shape anisotropy of the nanomagnets (see Methods). Each vertex

is associated with four nanomagnets oriented at a 90° angle with respect to each other and the net magnetisation is the sum of the individual magnetisation vectors of the four elements within a vertex. We observe that, after applying and removing a sufficiently large external field to saturate the array (see Methods), the thermally activated relaxation at room temperature is characterized by the rotation of the net magnetisation at the individual vertices in a unique direction: from state A to state B, as illustrated in Fig. 1. No statistically significant fraction of the vertices evolves from state A to state D, thus defining a ratchet in which the magnetostatic energy supplied by the saturating field is transformed into the clockwise rotation of the average magnetisation. This is a realisation of active matter: an out of equilibrium system that locally converts energy into directed motion[20,21]. In thermal equilibrium, a preferred direction of rotation does not occur due to microscopic reversibility. Chiral evolution is however possible if the system is far from equilibrium and in the presence of an asymmetric potential[22]. Using micromagnetic simulations, we find that an asymmetry is indeed generated in our system as a result of the topology of the stray field of the nanomagnet array. At the edges of the array, the stray field gives rise to emergent patterns, whose specific rearrangement during the thermal evolution can decrease the energy of the system, reminiscent of the role of magnetic surface charges in a ferromagnet. It is the energy decrease that accompanies the reordering of these ‘emergent charges’ that drives the chiral dynamics of the system during the thermal relaxation. Moreover, in the presence of a small bias field, heating allows the vertices to evolve into state C (Fig 1).

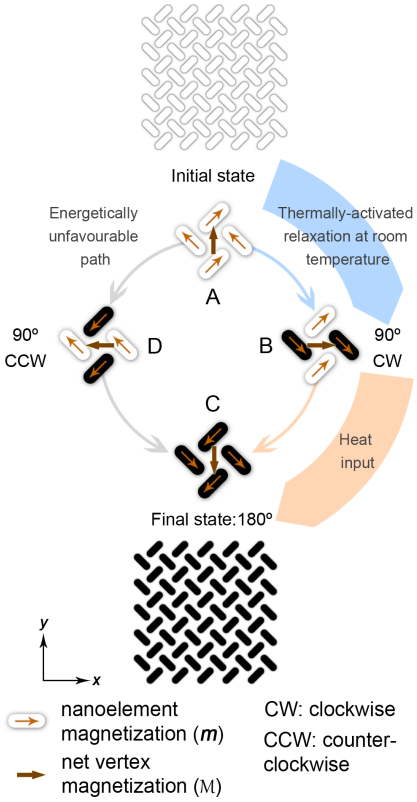

Fig. 1: Schematic representation of the chiral ice and evolution of the net magnetization at individual vertices within the array. The thermally activated evolution after initial saturation along the +*y* direction (state A) is illustrated, with the white or black colour, respectively indicating the direction of the magnetisation ***m*** toward the positive or negative *y* axis. The thin orange arrows represent the magnetization within the nanoelements while the net magnetisation at each individual vertex, M, is indicated by the large brown arrows at the centre of the vertices. The thermal relaxation at room temperature takes place stepwise via a clockwise (CW) rotation of the net magnetisation by 90° to state B and is indicated by the blue arrows. When the system is heated above room temperature in the presence of a bias field, the average magnetisation can locally rotate further (orange arrows), to state C. Considering the evolution from state A, state D statistically occurs with very low probability. The net vertex magnetisation therefore consistently rotates clockwise.

The experimental system consists of a finite array of elongated Permalloy nanomagnets arranged on a square grid as shown in Fig. 2a. An image of the full array is shown in Supplementary Information S1. We combine photoemission electron microscopy (PEEM) with x-ray magnetic circular dichroism (XMCD) to image the magnetic state of the individual nanomagnets. In the XMCD images (Fig. 2b), the nanomagnets in which the magnetisation is parallel to the propagation direction of the x-rays display a bright contrast, whereas nanomagnets in which the magnetisation is

reversed display a dark contrast. The homogeneous XMCD contrast for each nanomagnet confirms that they are in a single-domain state. The nanomagnets are sufficiently thin (see Methods), such that thermal energy can overcome the energy barrier to switch between the two possible single domain states at room temperature. The thickness is chosen so that the switching rates are comparable to the PEEM measurement time scale[23,24]. We first apply a saturating magnetic field, $\boldsymbol{H}_{\mathrm{sat}}$ (see Methods), such that, after its removal, the average remanent magnetisation of the array points along the positive *y* direction (Fig. 2c, where all nanomagnets display a bright contrast). The measured time evolution of the magnetisation over a period of 21 hours is shown in Fig. 2d-h in the presence of a weak bias field, as indicated in Fig. 2 (see Methods). The formation of regions with 'checkerboard' magnetic contrast pattern observed in Fig. 2d indicates that the average magnetisation at these vertices has evolved from state A to state B (see also Fig. 2b for a detailed view of state B), and have hence rotated by 90° in the clockwise (CW) direction. The evolution slows down considerably after ca. 4 hours, indicating that the system approaches thermal equilibrium, as explained in Supplementary Information S2. Heating the sample by a few Kelvin ensures that the thermal evolution, and therefore the rotation of vertices from state A to B, continues while vertices already in state B evolve into state C (dark contrast regions in Fig. 2e where the net magnetisation has locally rotated by 180°).

Throughout the evolution, the rotation of the net vertex magnetisation M (see Fig. 2b) starts at the edges of the array and propagates towards its centre. The heat-assisted rotation continues until the magnetisation in the array has mostly rotated by 180° with respect to state A (Fig. 2h). The quantitative evolution of the different vertex types (A, B and C) as well as the heating schedule are shown in Supplementary Information S3.

To confirm that the observed chiral behaviour is a magnetostatically-driven effect, we performed similar measurements on systems with a larger relative distance between nanomagnets, in which the strength of the magnetostatic interaction was reduced, and

found that the thermal evolution became achiral (see Supplementary Information S4). We also note that we did not observe any preferred direction of rotation in structures consisting of a single vertex with four nanomagnets, despite their structural chirality. A chiral structure by itself is therefore not sufficient to generate the observed dynamics: in the following we show that the dynamics is driven by the existence of an emergent asymmetric magnetostatic energy landscape.

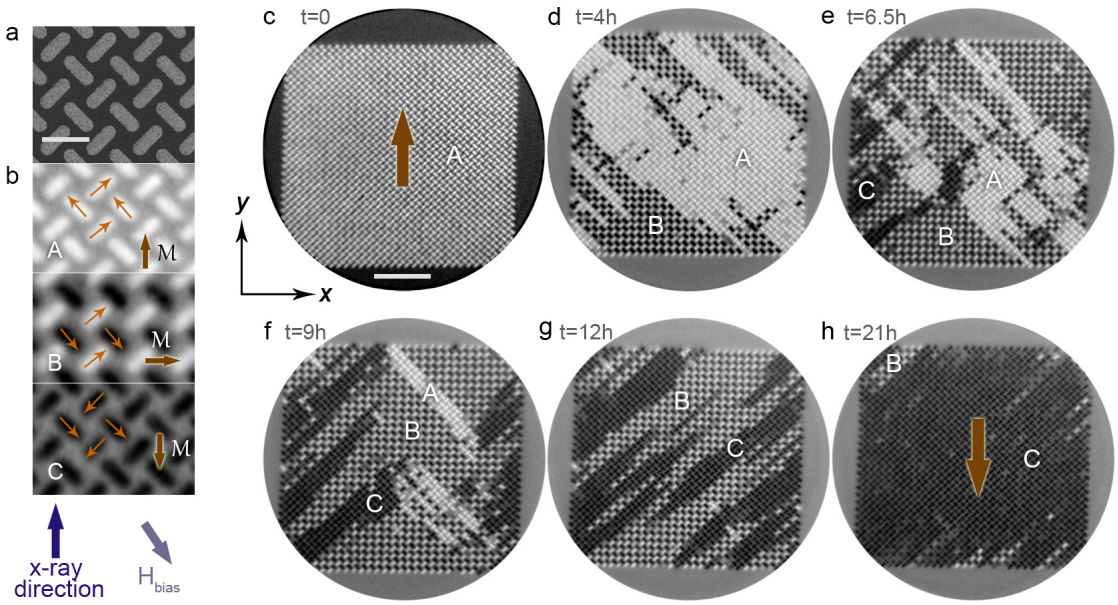

Fig. 2: Measured clockwise evolution of the magnetisation following saturation along the +*y* direction. (a) Top: Scanning electron microscopy (SEM) image of a region of the investigated array. The scale bar represents 600 nm. (b) XMCD contrast for states A, B and C, with arrows showing the orientation of the magnetisation for selected nanomagnets and the net vertex magnetisation in each case, indicated with a larger brown arrow and denoted M. (c) XMCD image of the array following saturation along the +*y* direction. The vertices are in state A with the average magnetisation within the array indicated by the large brown arrow. The detailed magnetic configuration of state A is shown in (b). The scalebar represents 5 μm and the field of view is of 25 μm. The contrast was adjusted for better visibility. (d-h) Time evolution of the magnetisation in the presence of a bias field. The magnitude of $\boldsymbol{H}_{\text{bias}}$ is between 50 μT and 80 μT, in the indicated direction. In (d), thermal relaxation at room temperature gives rise to domains of vertices in state B, mainly nucleating from the array edges and whose detailed magnetic configuration is shown in (b). The sample temperature was subsequently increased by a few Kelvin for four hours to ensure that the magnetisation reversals continue, as seen in (e-g). In (e), domains of vertices in state C [shown in panel (b)] nucleate from the edges of the array. Around t = 15 hours, the sample was heated again to achieve a close-to-complete 180° reversal of the magnetisation, observed in (h).

We performed micromagnetic simulations to qualitatively understand why the clockwise evolution of the magnetisation is favoured over the counterclockwise

147 evolution. The simulated system is a finite system identical to the one shown in Fig. 1,
148 with the same geometry as the experimentally studied one, but with fewer magnets
149 due to the computational cost of simulating the entire experimental array (see
150 Methods). We consider the system without the bias field in order to determine its
151 intrinsic thermal behaviour. Fig. 3a is a close-up of a section of the simulated array,
152 following saturation and removal of the field $\boldsymbol{H}_{\mathbf{sat}}$ (equivalent to state A in Fig. 2)**.** The
153 magnetostatic volume charges, $\rho = -\boldsymbol{\nabla} \cdot \boldsymbol{M}$, are plotted inside the nanomagnets along
154 with the generated stray field outside the nanomagnets. The stray field displays a
155 complex topology owing to the presence of antivortex patterns. Antivortices are two-
156 dimensional structures characterised by a field distribution in which the direction of the
157 field revolves clockwise around a central point[25] as schematically illustrated in the inset
158 of Fig. 3a, where the centre of the structure is indicated with an orange dot. Because
159 antivortices typically occur inside ferromagnets, we refer to the observed stray field
160 patterns as *virtual* antivortices, *i.e.* whose centre is located outside the nanomagnets[26].
161 Such virtual structures have previously been reported to play a role in the stability of
162 magnetisation patterns[25] as well as in the dynamics of coupled systems[27]. Considering
163 the entire simulated array (Fig. 3b), the distribution of the virtual antivortices within the
164 system following saturation is plotted in Fig. 3c. The overall stray field topology
165 effectively forms a virtual antivortex crystal, in which the antivortices, represented by
166 orange dots, display an ordered arrangement within the bulk of the array. At the edges,
167 the distribution of the virtual antivortices breaks the symmetry of the bulk arrangement.
168 Moreover, the distribution of the virtual antivortices along the horizontal edges (top and
169 bottom; highlighted in blue) is different from the distribution along with the vertical
170 edges (left and right; highlighted in red). The virtual antivortex distribution for a partial
171 clockwise rotation of the vertex magnetisation by 90° (state B) along four diagonals of
172 the array is given in Fig 3d. This corresponds to the magnetic state labelled ‘CW 1’ in
173 Fig. 3f where the four diagonals can be seen and is representative of experimentally
174 observed configurations. Within the bulk of the simulated array, the arrangement of the

virtual antivortices is modified: in domains where the net vertex magnetisation has rotated by 90° (dark grey regions), the antivortex stray field patterns are also rotated by 90°. At the edges of such domains (light grey regions), the antivortices are rotated by 45°, mirroring the rotation of the average magnetisation of those vertices. It is, however, along the array edges that the most significant changes take place: while the number of virtual antivortices remains constant, they have been rearranged compared to Fig. 3c. This is analogous to the situation in a finite-sized ferromagnet, where the stray field energy can be minimised through the rearrangement of surface charges, $\sigma = \boldsymbol{M} \cdot \boldsymbol{n}$ (where $\boldsymbol{n}$ is a normal vector to the surface), and result in the formation of domains within the ferromagnet. The rearrangement of the virtual antivortices in alternating patterns along the array edges is thus reminiscent of the pole avoidance principle in ferromagnets, which leads to the minimization of the magnetostatic energy through a reduction of the total magnetic charge. In the studied system the virtual antivortices thus function as emergent surface charges whose rearrangement, through the rotation of the magnetisation, minimises the total energy of the system during relaxation. In Fig. 3e, the emergent charge distribution is given for a system with four diagonals along which the average magnetisation has rotated counterclockwise. This distribution corresponds to the magnetic state labelled ‘CCW 1’ in Fig. 3f, where the vertices along those diagonals are in state D (see Fig. 1). When compared to Fig. 3d, the overall virtual antivortex structure is generally mirrored (along an axis defined by the saturation direction, *y*), except at the edges, where their distribution is not mirrored. Our simulations show that these differences lead to an asymmetric energy landscape in which the energy of the system decreases more efficiently through the clockwise (CW) rotation of the net vertex magnetisation at the edges than through the counterclockwise (CCW) rotation. We plot in Fig. 3f the relative difference in energy barriers at 300 K between the initial state (Fig. 3c) and the states in Figs. 3d and e, which are labelled as ‘CW 1’ and ‘CCW 1’. The energy barrier to access the clockwise state is lower, thus making it more probable. The energy barriers are also plotted for

configurations in which nanomagnets at the edges of the array have not switched. We find that, in these cases, the energy barriers for the clockwise and counterclockwise rotations of the net vertex magnetisation become equal. These results demonstrate that the chiral behaviour is driven by the edges of the system and that the observed initial clockwise rotation of the net vertex magnetisation following saturation is due to the intrinsically asymmetric energy landscape of the system.

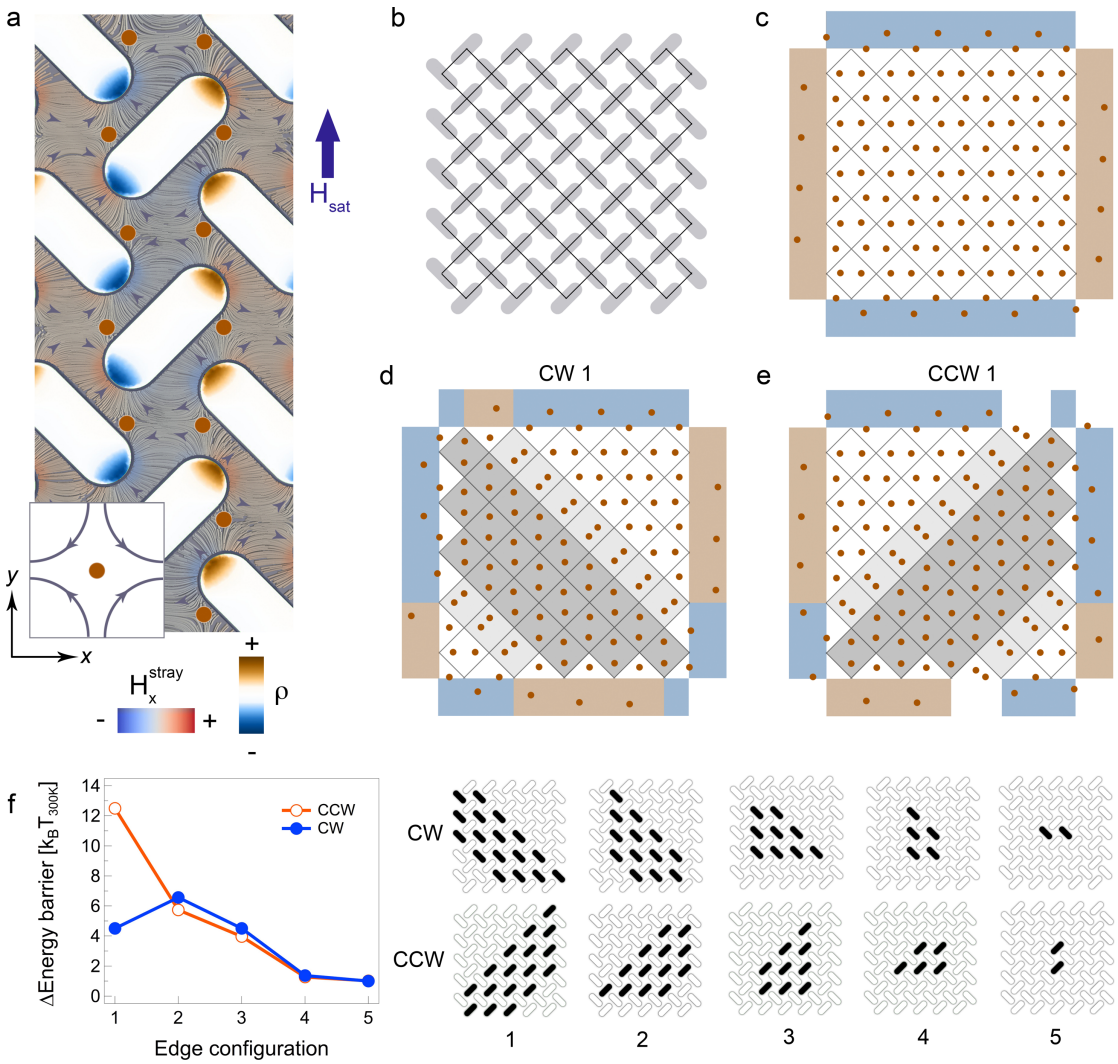

Fig. 3: Simulated stray field structure and energy barriers for clockwise and counterclockwise rotations of the average magnetisation. (a) Stray field configuration for a portion of the simulated nanomagnet array in state A, following saturation with the field $\boldsymbol{H}_{sat}$. The centres of the virtual antivortices are highlighted by orange dots and the magnetic volume charges (ρ) within the single-domain nanomagnets are plotted using the blue-brown colormap. The *x* component of the stray field, H_x^{stray}, is indicated by the blue-red colormap. An antivortex structure is schematically shown in the bottom inset. (b) Wire frame representation of the array lattice. (c) Distribution of the virtual antivortices (orange dots) in

the array in state A, following saturation along the +*y* direction. The different antivortex distributions along the array edges are highlighted in red and blue. In (d), the virtual antivortex distribution is plotted for a configuration in which the net magnetisation along four diagonals (dark grey regions) was rotated clockwise by 90° (state B). The corresponding magnetic state of the array is given in (f): configuration 'CW 1'. (e) Virtual antivortex distribution for a configuration in which the net vertex magnetisation along four diagonals is rotated counterclockwise by 90°, corresponding to the magnetic state 'CCW 1' in (f). In the white regions along the array edges in (e), the stray field distribution is identical to the one in the bulk. (f) Relative energy barriers, starting from the remanent state (a), for the shown configurations 1 – 5 in which the reversal of the magnetisation in edge nanoelements is gradually set back. The nanomagnets in black have switched (see Fig. 1 for colour convention). The energies are normalized to the barrier required to switch two nanomagnets in configuration 5, where the barrier is the same for the CW and CCW rotations.

The evolution of the average magnetisation during relaxation at room temperature eventually leads to thermal equilibrium. The measured continuous clockwise evolution of the magnetisation in the experiment towards state C is thus enabled by the bias field, which effectively modifies the energy landscape, such that the system can access state C upon moderate heating. We have also found that the bias field can, in some cases, be used to reverse the sense of rotation of the net vertex magnetisation. Indeed, after saturating a system with identical geometry to the one in Fig. 2 (see Methods) along the –*y* direction (Fig. 4a) we observe that, in the presence of $\boldsymbol{H}_{\text{bias}}$, the thermal evolution can proceed through the counterclockwise rotation of the net vertex magnetisation (Fig. 4b-d). Depending on the saturation direction, it is thus in principle possible to use a bias field to reinforce the 'built-in' clockwise rotation or to favour the counterclockwise sense of rotation of the average magnetisation.

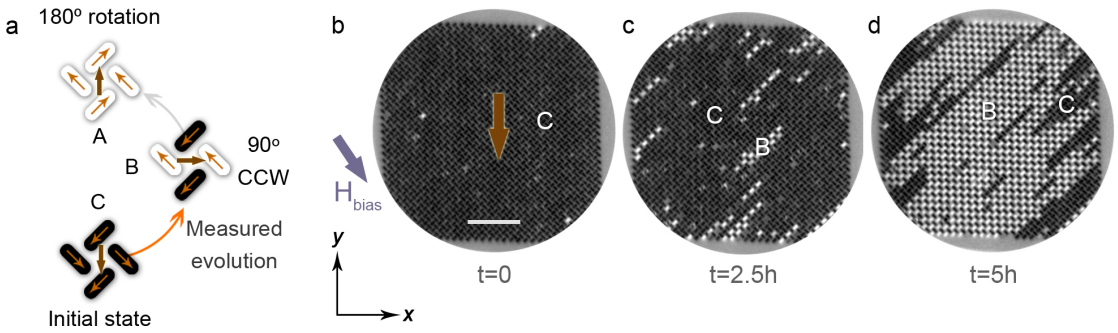

Fig. 4: Counterclockwise evolution of the system following saturation in the –*y* direction. (a) After saturating the array along the –*y* direction, the magnetisation evolves counterclockwise, *i.e.* from state C to state B (orange arrow), in the presence of the bias field $\boldsymbol{H}_{\text{bias}}$. (b-d) Measured time-evolution of the magnetisation. In (b), the array is in state C after saturation and the average magnetisation is indicated

by the large brown arrow. The evolution towards the sate shown in (c) occurs at room temperature. By heating the sample for 2.5 hours, the state shown in (d) can be accessed. The rotation from state B to state A was not observed owing to the orientation of the bias field. We note that the counterclockwise rotation from state C to state B is observed in about 20% of the measured samples. Indeed, starting from state C, the counterclockwise evolution favoured by the bias field competes with the natural clockwise evolution of the system and can cause the array to remain, on average, in state C. The scalebar represents 5 μm.

The magnetostatic interaction offers a known route for symmetry breaking at the surface of ferromagnets that can lead to rich behaviour, such as surface and curvature-induced non-reciprocal spin wave[28,29] and domain wall[30,31] propagation. Similarly, in the studied artificial spin system the origin of the thermally activated unidirectional rotation of the average magnetisation is due to the dynamic rearrangement of emergent magnetic surface charges, which result from the geometry of the array edges, demonstrating how magnetostatically-coupled nanomagnet arrays can be designed to harness thermal fluctuations of the magnetisation. This opens the possibility of exploiting artificial spin ices with tailored edge geometry and field-tunable dynamics as functional, active materials within devices that convert heat into motion, such as mesoscopic motors[20,22] and rotors[32] or within hybrid multistacks, used for example for magnetic memory applications[33], where the chiral array would form the active layer in which the rotation of the magnetisation could be triggered by laser pulses.

Methods

Sample Fabrication

Finite arrays of Permalloy ($Ni_{83}Fe_{17}$) nanomagnets were prepared on a silicon (100) substrate using electron beam lithography in conjunction with thermal evaporation at room temperature and a base pressure of 2×10^{-7} mbar followed by lift-off. The evaporation resulted in a nanocrystalline Permalloy film, which was capped by a 3 nm aluminium layer to protect against oxidation. The Permalloy film was evaporated with a thickness gradient along the sample in order to ensure the presence of a thermally

active region at room temperature adequate for the PEEM measurements[24]. Array thicknesses were measured using Atomic Force Microscopy (AFM). The thermally active arrays in Fig. 2 and 4 had identical geometries and were manufactured from nanomagnets with length and width of 470 nm and 170 nm, and with a lattice constant of 425 nm (centre-to-centre distance of neighbouring nanomagnets: see Supplementary Information S1). The measured thickness of the arrays was: 2.2 nm in Fig.1 and 2.7 nm in Fig. 4. The thicknesses were uniform across each array. The magnetisation in both arrays rotated clockwise after saturating along the +*y* direction, demonstrating that the thickness variation between the arrays did not affect the sense of rotation of the magnetisation. The array in Supplementary Information S3 had a thickness of 2.4 nm. The chiral structure of the system is defined by the geometry of the array edges as well as by its two-dimensional character where the shape anisotropy induced by the low Permalloy thickness ensures that the magnetisation is confined to the plane of the sample.

Experiment

Magnetic imaging was carried out with the photoemission electron microscopy endstation[34] at the Surface/Interface: Microscopy (SIM) beamline of the Swiss Light Source, Paul Scherrer Institute and at the PEEM-3 photoemission electron microscope at beamline 11.0.1 of the Advanced Light Source, Berkeley National Laboratory. Employing XMCD, the system was imaged by tuning the x-ray energy to the Fe L_3-edge. The magnetic contrast images were obtained by pixelwise division of two consecutive images recorded with right and left circular polarizations. The resulting contrast is proportional to $\boldsymbol{k} \cdot \boldsymbol{m}$, where $\boldsymbol{k}$ is the propagation vector of the x-rays and $\boldsymbol{m}$ the local magnetisation vector[35]. The sample orientation was optimized to maximize the contrast. The uniform contrast within the nanomagnets indicates that they were in a single-domain state. Nanomagnets with grey contrast were switching faster than the

measurement time. For observations of the magnetisation reversal at the Swiss Light Source, the samples were mounted on a copper (nonmagnetic) holder that allowed radiative heating of the sample and the temperature was measured using a PT100 sensor placed close to the sample. During the experiments the sample was exposed to a small constant bias field ($\boldsymbol{H}_{\text{bias}}$) with an estimated in-plane magnitude of 50 – 80 μT based on Hall probe measurements. The arrays were saturated *in-situ* using a permanent magnet inserted into the PEEM chamber. The saturating field strength at the location of the sample was of H_{sat}=15 mT in the plane of the sample. The magnet was retracted from the chamber after saturation. Measurements at the Advanced Light Source were carried out by saturating the sample both *ex-situ* as well as in a holder with a built-in electromagnet, which allowed us to apply fields up to 20 mT.

Micromagnetic simulations

Fully three-dimensional micromagnetic simulations based on a hybrid finite-element/boundary-element method[36,37] have been carried out on a system of 60 nanomagnets, each with lateral dimensions 235 nm × 85 nm (50% of experimental size) and 2 nm thick. The structure was discretized using a tetrahedral mesh with an average edge length of 1 nm. The material parameters for Permalloy were: saturation polarization $\mu_0 M_S$ = 1 T, exchange constant A = 1.3 × 10^{-11} J/m and zero magnetocrystalline anisotropy K = 0 J/m^3. The total Gibbs magnetic free energy is given by:

$$E(\boldsymbol{m}) = \int \left(A \left[\sum_{k}^{x,y,z} (\nabla m_k)^2 \right] + K[1 - (\boldsymbol{m} \cdot \boldsymbol{a})^2] - \frac{1}{2}\mu_0 M_S (\boldsymbol{H}_{\text{dem}} \cdot \boldsymbol{m}) \right.$$

$$\left. - \mu_0 M_S (\boldsymbol{H}_{\text{ext}} \cdot \boldsymbol{m}) \right) dV.$$

E is the sum of the exchange energy, the anisotropy energy, the demagnetising energy, and the Zeeman energy. $\boldsymbol{m} = \boldsymbol{M}/M_S$ is the reduced magnetisation, A is the

exchange constant, K the magnetocrystalline anisotropy, $\boldsymbol{a}$ is a unit vector along the magnetocrystalline anisotropy direction, $\boldsymbol{H}_{dem}$ is the demagnetising field and $\boldsymbol{H}_{ext}$ an external field. The integral is over the magnetic volume. In the performed simulations $H_{ext}=0$.

To understand the thermal stability and transition probability from the remanent state, following the application of a saturating field, to different magnetic states, *i.e.* configurations resulting from clockwise and counterclockwise rotations, we used the nudged elastic band method to find the lowest possible energy transition path between the two states[38]. We start from a magnetisation state, $\boldsymbol{M}_1$, where the magnetic system occupies a local minimum. Through thermal activation, the system can overcome the local energy barrier and move towards a different minimum state, $\boldsymbol{M}_2$, following either clockwise or counterclockwise rotation of the vertex magnetisation. The difference between the local minima and the saddle point in the energy path gives the energy barrier that has to be overcome to move to the next local minima; this determines the stability of the magnetic state. An optimization algorithm is applied until, at any point along the path, the gradient of the energy is only pointing along the path. This represents the path with the greatest statistical weight. The state with the lowest energy barrier has the highest probability of being reached.

Data availability

The data that support the findings of this study are available from the corresponding author S.G. upon reasonable request.

Contributions

RLS and SG conceived the spin ice geometry and the experiment. SG, AF, CD and JC prepared the samples. SG, CD, JC, JB, AK, AF, RC, EK, AS, and NB performed the experiments and analysed the experimental data. GH, SG and JB performed and

evaluated the micromagnetic simulations. SG, RLS, GH, JB, CD, AK, YM and LJH interpreted the results. SG wrote the manuscript with input from all coauthors. All authors discussed the results and commented on the manuscript.

Acknowledgements

The authors thank Oles Sendetskyi, Hanu Arava, Vitaliy Guzenko, Eugen Deckardt and Jeroen Bosgra for technical assistance. SG wishes to thank Naëmi Leo and Anthony Arrott for helpful discussions as well as Sandra Arnold for advice with the graphics in the manuscript and Michael Sternberg for support with the High-Performance Computing Cluster at the Center for Nanoscale Materials. RLS thanks Fabio Nascimento for discussions. SG was funded by the European Union's Horizon 2020 research and innovation programme under the Marie Sklodowska-Curie grant agreement No. 708674. The work of GH was supported by the EPSRC (grants EP/M015173/1 and EP/L019876/1), the Vienna Science and Technology Fund under WWTF Project MA14-44 and the Royal Society under Grant No. UF080837. The work of RLS was supported by the EPSRC (grants EP/L002922/1 and EP/M024423/1). AF was supported by the Swiss National Science Foundation. Part of this work was performed at the Surface/Interface: Microscopy (SIM) beamline of the Swiss Light Source, Paul Scherrer Institut, Villigen, Switzerland. This research used resources of the Advanced Light Source, which is a DOE Office of Science User Facility under contract no. DE-AC02-05CH11231. Use of the Center for Nanoscale Materials, an Office of Science user facility, was supported by the U.S. Department of Energy, Office of Science, Office of Basic Energy Sciences, under Contract No. DE-AC02-06CH11357.

The authors have no competing financial interests.

References

1. Wang, R. F. *et al.* Artificial ‘spin ice’ in a geometrically frustrated lattice of nanoscale ferromagnetic islands. *Nature* **439,** 303–306 (2006).
2. Heyderman, L. J. & Stamps, R. L. Artificial ferroic systems: novel functionality from structure, interactions and dynamics. *Journal of Physics: Condensed Matter* **25,** 363201 (2013).
3. Morrison, M. J., Nelson, T. R. & Nisoli, C. Unhappy vertices in artificial spin ice: new degeneracies from vertex frustration. *New Journal of Physics* **15,** 045009 (2013).
4. Mengotti, E. *et al.* Real-space observation of emergent magnetic monopoles and associated Dirac strings in artificial kagome spin ice. *Nature Physics* **7,** 68–74 (2010).
5. Vedmedenko, E. Y. Dynamics of Bound Monopoles in Artificial Spin Ice: How to Store Energy in Dirac Strings. *Physical Review Letters* **116**, 077202 (2016).
6. Gilbert I, *et al.* Emergent ice rule and magnetic charge screening from vertex frustration in artificial spin ice. *Nature Physics* **10**, 670 (2014).
7. Farhan, A. *et al.* Thermodynamics of emergent magnetic charge screening in artificial spin ice. *Nature Communications* **7**, 12635 (2016).
8. Branford, W. R., Ladak, S., Read, D. E., Zeissler, K. & Cohen, L. F. Emerging Chirality in Artificial Spin Ice. *Science* **335,** 1597–1600 (2012).
9. Le, B. *et al.* Understanding magnetotransport signatures in networks of connected permalloy nanowires. *Physical Review B* **95**, 060405(R) (2017).
10. Gliga, S., Kákay, A., Hertel, R. & Heinonen, O. G. Spectral Analysis of Topological Defects in an Artificial Spin-Ice Lattice. *Physical Review Letters* **110,** 117205 (2013).
11. Jungfleisch, M. B. et al. Dynamic response of an artificial square spin ice. *Physical Review B* **93**, 100401(R) (2016).

12. Bhat, V. S, Heimbach, F., Stasinopoulos, I. and Grundler D. Magnetization dynamics of topological defects and the spin solid in a kagome artificial spin ice. *Phys. Rev. B* **93**, 140401(R) (2016).

13. Kelly, T. R., De Silva, H. & Silva, R. A. Unidirectional rotary motion in a molecular system. *Nature* **401**, 150–152 (1999).

14. Mochizuki, M. *et al*. Thermally driven ratchet motion of a skyrmion microcrystal and topological magnon Hall effect. *Nature Materials* **13**, 241 (2014).

15. Gansel, J. K. et al. Gold helix photonic metamaterial as broadband circular polarizer. *Science* 325, 1513–1515 (2009).

16. Bode, M. *et al.* Chiral magnetic order at surfaces driven by inversion asymmetry. *Nature* **447**, 190–193 (2007).

17. Zakeri, Kh. *et al*. Asymmetric Spin-Wave Dispersion on Fe(110): Direct Evidence of the Dzyaloshinskii-Moriya Interaction. *Physical Review Letters* **104**, 137203 (2010).

18. Barron, L. D. TRUE AND FALSE CHIRALITY AND PARITY VIOLATION. *Chemical Physics Letters* **123,** 423–427 (1986).

19. Hel-Or, Y., Peleg, S. & Avnir, D. Two-Dimensional Rotational Dynamic Chirality and a Chirality Scale. *Langmuir* **6,** 1691–1695 (1990).

20. Browne, W. R. & Feringa, B. L. Making molecular machines work. *Nature Nanotechnology* **1,** 25–35 (2006).

21. Romanczuk, P., Chaté, H., Chen, L., Ngo, S. & Toner, J. Emergent smectic order in simple active particle models. *New Journal of Physics* **18,** 063015 (2016).

22. Hänggi, P. & Marchesoni, F. Artificial Brownian motors: Controlling transport on the nanoscale. *Reviews of Modern Physics* **81**, 387–442 (2009).

23. Kapaklis, V. et al. Thermal fluctuations in artificial spin ice. *Nature*

Nanotechnology **9**, 514–519 (2014).

24. Farhan, A. *et al.* Exploring hyper-cubic energy landscapes in thermally active finite artificial spin-ice systems. *Nature Physics* **9,** 1–8 (2013).

25 Gliga, S., Hertel, R. & Schneider, C. M. Switching a magnetic antivortex core with ultrashort field pulses. *Journal of Applied Physics* **103,** 07B115 (2008).

26. Dotse, D. & Arrott, A. A.. Micromagnetic studies of vortices leaving and entering square nanoboxes. *Journal of Applied Physics* **97**, 10E307 (2005).

27. Kumar, D., Barman, S. & Barman, A. Magnetic Vortex Based Transistor Operations. *Sci. Rep.* **4,** 4180 (2014).

28. Camley, R. E. Nonreciprocal surface waves. *Surface Science Reports* **7,** 103–187 (1987).

29. Otálora, J. A., Yan, M., Schultheiss, H., Hertel, R. & Kákay, A. Curvature-Induced Asymmetric Spin-Wave Dispersion. *Physical Review Letters* **117,** 227203 (2016).

30. Yan, M., Andreas, C., Kákay, A., Garcia-Sanchez, F. & Hertel, R. Chiral symmetry breaking and pair-creation mediated Walker breakdown in magnetic nanotubes. *Applied Physics Letters* **100,** 252401 (2012).

31. Hertel, R. CURVATURE-INDUCED MAGNETOCHIRALITY. *SPIN* **03,** 1340009 (2013).

32. Fletcher, S. P., Dumur, F., Pollard, M. M. & Feringa, B. L. A Reversible, Unidirectional Molecular Rotary Motor Driven by Chemical Energy. *Science* **310,** 80–82 (2005).

33. Wong, H.-S. P. & Salahuddin, S. Memory leads the way to better computing. *Nature Nanotechnology* **10**, 191 (2015).

34. Le Guyader, L. *et al*. Studying nanomagnets and magnetic heterostructures with X-ray PEEM at the Swiss Light Source. Journal of

Electron Spectroscopy and Related Phenomena **185**, 371-380 (2012).

35. Stöhr, J. *et al.* Element-Specific Magnetic Microscopy with Circularly Polarized X-rays. *Science* **259,** 658–661 (1993).

36. Chantrell, R. W., Fidler, J., Schrefl, T., & Wongsam, M. Micromagnetics: Finite Element Approach, in *Encyclopedia of Materials: Science and Technology* p. 5651-5660 (Elsevier, 2001).

37. Hertel, R. Guided Spin Waves, in *Handbook of Magnetism and Advanced Magnetic Materials*. (John Wiley & Sons, 2007).

38. Dittrich, R. *et al.* A path method for finding energy barriers and minimum energy paths in complex micromagnetic systems. *Journal of Magnetism and Magnetic Materials* **250,** L12 (2002).